Revision 2

Ferric-ferrous iron ratios of experimental majoritic garnet and clinopyroxene as a function of oxygen fugacity

Authors:

Laura J. A. Rzehak[1,2]* (Laura.Rzehak@rub.de), **Arno Rohrbach[2]** (arno.rohrbach@uni-muenster.de), **Christian Vollmer[2]** (christian.vollmer@uni-muenster.de), **Heidi E. Höfer[3]** (hoefer@em.uni-frankfurt.de), **Jasper Berndt[2]** (jberndt@nwz.uni-muenster.de), **Stephan Klemme[2]** (stephan.klemme@uni-muenster.de)

[1] Ruhr Universität Bochum, Institut für Geologie, Mineralogie und Geophysik, Universitätsstraße 150, 44780 Bochum

[2] Westfälische Wilhelms-Universität Münster, Institut für Mineralogie, Corrensstraße 24, 48149 Münster

[3] Goethe Universität Frankfurt am Main, Institut für Geowissenschaften, Altenhöferallee 1, 60438 Frankfurt am Main

* corresponding author: Laura.Rzehak@rub.de

Abstract

The oxidation state of iron in upper mantle minerals is widely used to constrain the Earth mantle's oxidation state. Previous studies showed high levels of ferric iron in high-pressure majoritic garnets and pyroxenes despite reducing conditions. To disentangle the effects of pressure and increasing oxygen fugacity on the $Fe^{3+}/\Sigma Fe$ ratios of garnet and clinopyroxene, we performed high-pressure experiments at pressures of 10 GPa in a 1000-ton Walker-type multi-anvil apparatus at the University of Münster. We synthesized majoritic garnets and clinopyroxenes with a total iron content close to natural mantle values at different oxygen fugacities, ranging from IW+4.7 to metal saturation at IW+0.9. We analyzed the iron oxidation state in garnets with the electron microprobe "flank method". Furthermore, we investigated the oxidation state of iron in garnets and clinopyroxenes with transmission electron microscopy (TEM) electron energy loss spectroscopy (EELS). Although the flank method measurements are systematically lower than the EELS measurements, $Fe^{3+}/\Sigma Fe$ obtained with both methods agree well within 2σ errors. The "flank method" has the advantage of being much faster and more easily to set-up, whereas TEM-EELS has a much higher spatial resolution can be applied to a variety of non-cubic minerals such as orthopyroxenes and clinopyroxenes. We used our experimental results to compare two geobarometers that contain a term for ferric iron in garnet (Beyer and Frost 2017, Tao et al. 2018) with two geobarometers that do not account for ferric iron (Collerson et al. 2010, Wijbrans et al. 2016). We found that garnets with low total Fe and Fe^{3+} (like many natural garnets) pressures can be calculated without including the ferric iron content.

Keywords

majorite, multi anvil apparatus, electron energy loss spectroscopy, transmission electron microscopy, flank method, ferric iron, oxygen fugacity, Earth mantle

Introduction

The oxidation state of the Earth's upper mantle is still a matter of debate, mainly because rock samples from depths > 250 km are virtually absent except for rare ultradeep xenoliths (Haggerty and Sautter 1990; Sautter et al. 1991) and mineral inclusions in diamond (e.g. Pearson et al. 2014). However, the oxidation state of the Earth's mantle exerts a significant influence on the stability of C-O-H-volatiles and therefore has important implications for the phase relations and melting behavior (Kushiro et al. 1968; Taylor and Green 1988; Ballhaus and Frost 1994; Gaetani and Grove 1998; Dasgupta and Hirschmann 2006; Foley 2011; Tumiati et al. 2012; Stagno et al. 2013), hydrogen incorporation (e.g. Kohlstedt et al. 1996) and the rheology of the mantle (Mackwell et al. 1985,) as well as for diamond/graphite vs. carbonate stability (Dasgupta and Hirschmann 2010; Stagno and Frost 2010; Rohrbach and Schmidt 2011; Stagno et al. 2013; Luth and Stachel 2014; Yaxley et al. 2017). The oxidation state of the upper mantle can be determined by the $Fe^{3+}/\Sigma Fe$ content of mantle minerals since iron is a major element in Earth's mantle and is incorporated into every mantle mineral (e.g. O'Neill et al. 1993b; Luth and Canil 1993; Canil and O'Neill 1996). The oxygen fugacity (fO_2) of the uppermost mantle predominantly lies between FMQ+2 and FMQ-2 as indicated by xenoliths and samples of basaltic melts and peridotite massifs (Luth et al. 1990; Ballhaus 1993; Frost and McCammon 2008). With increasing depth, the upper mantle becomes more reduced, approaching $\Delta \log fO_2$ values of FMQ-4 at 220 km depth (Woodland and Koch 2003; McCammon and Kopylova 2004; Frost and McCammon 2008; Stagno and Frost 2010; Yaxley et al. 2012). In the upper mantle the fO_2 correlates with the ferric iron content of minerals, so that spinels in harzburgite and lherzolite at pressures up to 2.7 GPa show a decrease of ferric iron with

decreasing fO_2 tending towards zero when metallic iron is a stable phase (Ballhaus et al. 1991). This linear relationship between fO_2 and $Fe^{3+}/\Sigma Fe$ is not observed in experimental phase assemblages at pressures corresponding to the lowermost upper mantle, the transition zone or the lower mantle, where majoritic garnet and bridgmanite with high ferric iron contents coexist with metallic iron (O'Neill et al. 1993a; McCammon 1997; McCammon and Ross 2003; Frost et al. 2004; Rohrbach et al. 2007; 2011). In a typical upper mantle assemblage, ferric iron is concentrated in modally minor phases like clinopyroxene and spinel since olivine incorporates negligible ferric iron and orthopyroxene incorporates only between 0.2 and 0.6 wt% Fe_2O_3 at low $Fe^{3+}/\Sigma Fe$ between 0.03 and 0.10 (O'Neill et al. 1993b; Canil and O'Neill 1996; Woodland and Koch 2003; Yaxley et al. 2012). Above 6 GPa, pyroxene components become more soluble in garnet and substitute continuously into the garnet structure (Akaogi and Akimoto 1979; Irifune 1989; Rohrbach et al. 2011; Wijbrans et al. 2016; Beyer and Frost 2017; Kiseeva et al. 2018). Assuming that the transition zone has the same bulk chemical composition as the upper mantle, including the $Fe^{3+}/\Sigma Fe$ content, the fO_2 of the transition zone consequently must depend on how well its minerals can incorporate ferric iron. Since most transition zone minerals can incorporate some ferric iron (see compilation in Frost and McCammon 2008), the average amount of around 2000 µg/g Fe_2O_3 (O'Neill et al. 1993a), will be partitioned into a wider range of minerals within the transition zone than in the upper mantle. This leads to a dilution effect and a decreased ferric iron activity, which results in decreased fO_2 (O'Neill et al. 1993a Ballhaus 1995). The presence of high amounts of ferric iron in transition zone majoritic garnet or in lower mantle bridgmanite in spite of low fO_2 can either be explained by a reduction of oxidized volatiles as CO_2 and H_2O to CH_4 or more likely, by disproportionation of $3Fe^{2+}O = Fe_2^{3+}O_3 + Fe^0$ (O'Neill et al. 1993a; Frost et al. 2004; Rohrbach et al. 2007).

In order to track redox conditions of the upper mantle and the transition zone, ferric iron contents of garnets have been used extensively. Garnet has several advantages, because it is stable over a wide range of pressures and temperatures from the upper mantle into the transition zone (e.g., Klemme and O'Neill 2000; Klemme and Fumagalli, 2015), and is consequently one of the most common rock-forming minerals of the Earth's interior (Ringwood 1967; Ringwood and Major 1971). Therefore, the incorporation of ferric iron in pyroxene-garnet solid solutions at high pressures has been repeatedly studied (McCammon and Ross 2003; Rohrbach et al. 2007; 2011; Beyer and Frost, 2017). All former studies agree about the onset of majorite stability in garnet solid solutions at around 6 GPa. Pyroxenes dissolve increasingly into the garnet structure to form majoritic garnet with increasing depth and consequently the majorite component can be used for geobarometry (Collerson et al. 2010; Wijbrans et al. 2016; Beyer and Frost 2017; Tao et al. 2018). Compared to regular garnets, where the dodecahedral site is occupied by divalent cations and the octahedral site by trivalent cations, majorites incorporate Si^{4+} and Mg^{2+} on the octahedral site.

In this study, we performed high-pressure multi-anvil experiments at different oxygen fugacities with a total iron content of 8 wt% reflecting the iron content of the mantle (Palme and O'Neill 2003). We quantified the ferric iron contents of our garnets and clinopyroxenes and used them to review several majorite geobarometers (Collerson et al. 2010; Wijbrans et al. 2016; Beyer and Frost 2017; Tao et al. 2018). The quantification of ferric iron was performed with two different methods using the same samples: transmission electron microscopy - electron energy loss spectroscopy (TEM-EELS; van Aken et al. 1998; van Aken and Liebscher 2002) and the electron microprobe (EPMA) flank method (Höfer 2002; Höfer and Brey 2007).

Experimental and analytical methods

The high-pressure experiments were performed with a synthetic starting material representing a primitive mantle composition (Palme and O'Neill 2003; Table 1). To increase the modal amounts of ferric iron-bearing minerals such as clinopyroxene and garnet, we subtracted 30 wt% olivine from that composition. We prepared a mixture of all elements except iron from high purity oxides and carbonates (Alfa Aesar) in an agate mortar under acetone. This mixture was decarbonated over night at 1000 °C. We then added reagent grade FeO (Alfa Aesar) to the mixture and homogenized the starting material again for 30 minutes in an agate mortar. The Mg# (Mg/(Mg+Fe); atoms per formula unit) of the starting material is 0.8 at a total FeO content of 8 wt%, to obtain phase compositions directly comparable to natural minerals. The downside of low FeO contents in minerals is a generally low count rate during TEM-EELS and EPMA measurements.

In order to constrain the relationship between the fO_2 and the $Fe^{3+}/\Sigma Fe$ for clinopyroxene and garnet, we synthesized these phases at different redox conditions between IW+0.9 and IW+4.7. The most reducing experiment at IW+0.9 (MaLm11) was performed by using a double capsule technique. The starting material was contained in a welded shut noble metal ($Au_{80}Pd_{20}$) inner capsule, which was surrounded by an outer iron metal capsule. The hydrogen source between the two capsules was brucite. In experiment MaLm6 we added 1 wt% Si metal to the starting material. This triggers a reaction of silicon metal and iron(II)oxide to metallic iron and silicon dioxide and reduces the intrinsic fO_2 of the sample (Tsuno et al. 2013). We fixed the fO_2 of the samples MaLm1 and MaLm2 to values close to the enstatite-magnesite-olivine-diamond (EMOD) buffer by adding 1 wt% graphite to our starting material (Eggler et al. 1979). Furthermore, 5 wt% stearic acid was added to all samples to produce a C-O-H fluid component (Sokol et al. 2010) at experimental P and T which lowers the intrinsic fO_2 of the composition and facilitates reaching equilibrium in subsolidus runs. The most oxidized experiments, where fO_2 was not buffered (MaLm9 and MaLm12), were performed in welded $Au_{80}Pd_{20}$ capsules. The experiments were performed

This is the peer-reviewed, final accepted version for American Mineralogist, published by the Mineralogical Society of America.
The published version is subject to change. Cite as Authors (Year) Title. American Mineralogist, in press.
DOI: https://doi.org/10.2138/am-2020-7265. http://www.minsocam.org/

between 1450 to 1550 °C at 10 GPa in a 1000-ton Walker-type multi-anvil apparatus at the University of Münster. All run conditions are presented in Table 2 and in the Supplementary material (Table S1). The experiments were performed using a 14/8 assembly (14 mm octahedron edge length, 8 mm truncated edge length) employing Cr-doped MgO octahedron and a zirconia insulating sleeve around a stepped $LaCrO_3$ furnace. For details regarding the pressure calibration of the press see Wijbrans et al. (2016). Run temperatures were measured with type C-thermocouples and controlled within ± 5°C by an Eurotherm controller. Experiments were quenched by turning off the power supply.

All samples were mounted in an acrylic resin and polished down to the center of the capsule. Backscattered electron images were performed with a JEOL JSM-6510LA scanning electron microscope at the University of Münster. Major and minor element analyses were performed with a JEOL JXA-8530F electron microprobe at the University of Münster using natural minerals as standards. The following standards were used for quantification: hypersthene (Si), disthene (Al), fayalite (Fe), olivine (Mg, Ni), diopside (Ca), jadeite (Na). For garnet analysis we used natural pyrope as standard for Si, Al and Mg. The EPMA acceleration voltage was 15 kV and the beam current was 15 nA. The spot sizes were 1-5 µm depending on the grain size. Counting times were 20 s on the peak and 10 s on the background for metals and garnets, for other silicates 15 s on the peak and 5 s on the background.

The EPMA flank method measurements of the garnets were performed with the JEOL JXA 8900RL Superprobe at Goethe University in Frankfurt. The measurements were carried out at an acceleration voltage of 15 kV, and a beam current of 120 nA and a beam diameter of 1 µm. Each $Fe^{3+}/\Sigma Fe$ determination with simultaneous major element analysis resulted from the average of 25 independent measurements on different grains to achieve an uncertainty of below 0.02 in $Fe^{3+}/\Sigma Fe$

(1σ). Counting times were 20 to 30 s on the peak and background for all main elements besides iron (60 s), and 140 s for each Fe$L\alpha$ and Fe$L\beta$ measurement. In general, the flank method combines measuring the shift of the peak position and the change in intensity ratios of Fe$L\alpha$ and Fe$L\beta$, which systematically varies with the $Fe^{3+}/\Sigma Fe$ content, resulting in the high sensitivity and high precision of this method (Höfer and Brey 2007). The garnet standards used to calibrate and to quantify $Fe^{3+}/\Sigma Fe$ in our samples contain between 6 and 21 wt% total iron: oxyAlm: 20.21 wt% ΣFe, 0.03 wt% $Fe^{3+}/\Sigma Fe$ (Höfer and Brey 2007; Vasilyev 2016); UA5: 6.49 wt% ΣFe, 0.11 $Fe^{3+}/\Sigma Fe$ (Vasilyev 2016; Li et al. 2018); UA17: 6.25 wt% ΣFe, 0.06 $Fe^{3+}/\Sigma Fe$ (Vasilyev 2016); Damknolle: 15.18 wt% ΣFe, 0.04 $Fe^{3+}/\Sigma Fe$ (Höfer and Brey 2007; Vasilyev 2016). $Fe^{3+}/\Sigma Fe$ of all garnet standards were measured by Mössbauer spectroscopy prior to the flank measurements (McGuire et al. 1992; Rankenburg et al. 2002; Höfer and Brey 2007). The empirically determined 1σ error is ± 0.02 for these samples (Höfer and Brey 2007). The flank method was already successfully used to quantify $Fe^{3+}/\Sigma Fe$ in garnets (Malaspina et al. 2009; 2010; Höfer and Brey 2007; Tao et al. 2018), sodic amphiboles (Enders et al. 2002) and wustites (e.g. Höfer et al. 2000). Furthermore, several groups are currently working on flank-method calibrations for other minerals and glasses (Malaspina et al. 2010; Zhang et al. 2018).

For TEM analysis, the former EMPA samples were prepared by ultramicrotomy, in order to avoid a change in their chemical composition, and put onto carbon-film copper TEM-grids. Preparation resulted in slices of 70 nm thickness, which is specifically important for EELS analysis to avoid multiple scattering effects. Although the mechanical stress induced by the diamond knife resulted in severe shattering of the samples, no chemical disturbance of analyzed minerals can be expected, perhaps in contrast to ion beam techniques. EELS measurements were performed on a Zeiss Libra 200FE TEM at the University of Münster equipped with a Schottky-type field emission gun (200

kV) and a Köhler illumination system providing strongly parallel illumination conditions at all brightness indices. Samples were initially documented by conventional Brightfield (BF) and Scanning TEM- High Angle Annular Darkfield (HAADF, contrast proportional to average Z) imaging. Energy filtering was performed through an in-column Omega filter in TEM mode using a 200 µm filter entrance aperture giving an effective aperture of about 100 nm on the sample surface. The energy spread of the field emitter is 0.7 eV as determined from the full width at half maximum of the zero loss peak (ZLP). Convergence angle was about 0.1 milliradian (quasi-parallel Köhler illumination). The following routine was used to record EELS spectra: First, the ZLP was recorded with a low brightness index to avoid damage of the slow-scan CCD camera Gatan UltraScan 4000 (5 frames at 0.1 or 0.2 s integration time). Afterwards, the Fe$L_{2,3}$ edge was recorded with a much higher brightness index and longer exposure times (10 frames at 5 s integration time). We analyzed up to 9 grains of garnet and clinopyroxene per sample, measurements with more than 2σ variation of the mean were considered as outliers and thus excluded from the calculation of the mean. Due to the required total iron content of at least several wt% it was only possible to measure three samples: the rather oxidized samples MaLm1 and MaLm9 and the metal saturated sample MaLm11. All EELS measurements were examined with the MATLAB® script EELSA (Prescher et al. 2014). EELSA uses the two basic procedures described by van Aken and Liebscher (2002). The first approach applies two 2 eV wide integration windows to the FeL_3 maximum (Fe^{3+}) and the FeL_2 maximum (Fe^{2+}) of the sample. By dividing the ferrous iron content at L_2 by the ferric iron content at L_3 the $Fe^{3+}/\Sigma Fe$ content of the sample can be determined from the spectrum. The second approach employs several Gaussian functions describing the spectral features and one Arctan function to fit the remainder of the EELS spectrum (van Aken and Liebscher 2002). Both approaches make use of the significant shapes of the Fe$L_{2,3}$ edges that depend on the valence state of iron. Minerals with simply divalent iron content show a sharp peak of their L_3 edge at 707.8 eV

and a weaker peak at 710.5 eV. Samples with trivalent iron only show a sharp peak of their L_3 edge at 709.5 eV with a weaker pre-peak at 708.0 eV (van Aken and Liebscher 2002). The difference between L_3 and L_2 edge is a result of spin-orbit splitting (Colliex et al. 1991; Garvie et al. 1994; van Aken et al. 1998). The absolute 1σ error of the quantification technique is ± 0.02 (van Aken and Liebscher 2002).

Results

Experimental results and phase compositions

Backscattered electron (BSE) images of typical run products from this study are shown in Figure 1. Olivine is the most abundant phase in our run products with modal amounts between 37 and 45 vol%. The second most abundant phase is majoritic garnet (22-39 vol%). Clinopyroxenes are present between 19 and 33 vol%, whereas orthopyroxene is only a minor phase (2 to 15 vol%). The modal proportions were calculated via mass balancing and agree well with the phase proportions observed in the scanning electron microscope (SEM) images. Most run products contain olivine, clinopyroxene, majoritic garnet and orthopyroxene, i.e. a regular mantle mineral assemblage. The mineral assemblages in MaLm2 and MaLm12 differ from the other samples such that MaLm12 contains little orthopyroxene and MaLm2 contains orthopyroxene, garnet, magnesite, diamond and carbonate/carbonatite melt but no olivine (Fig. 1a,b). The sample MaLm1 also contains small magnesite grains, but no related melt component. The appearance of carbonatite melt is most likely the result of adding stearic acid to the charges which produces minor amounts of CO_2 when it decomposes at high T in a starting material with high intrinsic fO_2. CO_2 could also result from incomplete decarbonation of the starting material, which would be rather beneficial to buffer fO_2 close to EMOD. The Mg# of all minerals are around 0.90 (Table 3). The Si-metal modified sample

MaLm6 contains olivine, orthopyroxene, clinopyroxene and garnet (Fig. 1c). The metal-saturated sample MaLm11 still contains the Ir-Fe alloy with high Fe content (Fig. 1d,e). Sample MaLm12 contains little orthopyroxene, but olivine, clinopyroxene and majoritic garnet (Fig. 1f). The phases throughout the charge are homogeneous in terms of chemical compositions and also when comparing different run products (Table 3 and Supplementary material Tables S2 and S3).

All garnets from this study are considered majoritic, since they contain more than three silicon cations per 12 oxygens. The composition of our majorites is a solid solution among majorite ($Mg_4Si_4O_{12}$), grossular ($Ca_3Al_2Si_3O_{12}$), almandine ($Fe_3Al_2Si_3O_{12}$), pyrope ($Mg_4Si_4O_{12}$) and andradite ($Ca_3Fe^{3+}{}_2Si_3O_{12}$) components (Supplementary material Table S2, after Locock 2008).

Garnets are more pyrope-rich and majorite-poor compared to garnets synthesized at 10 GPa by Rohrbach et al. (2011) due to the overall higher Mg# of our starting material. However, our garnets generally show a lower Mg# than the pyroxenes, which is consistent with results from previous studies (Rohrbach et al. 2007; 2011).

Orthopyroxenes generally have a higher Mg# (0.90-0.96) than the corresponding clinopyroxenes (0.88-0.97). All clinopyroxenes and orthopyroxene compositions are close to $Di_{86}Ja_{11}Ae_3$ and $En_{92}Fs_6Wo_2$.

Oxygen fugacity

Oxygen fugacities of all samples were monitored by adding 3 wt% iridium to all starting compositions as a redox sensor (Woodland and O'Neill 1997; Stagno and Frost 2010; Rohrbach and Schmidt 2011). During an experiment iron dissolves into the iridium metal which can be analyzed by EPMA (Supplementary material, Table S1). Oxygen fugacities were calculated using the method described in Rohrbach and Schmidt (2011). Uncertainties on the fO_2 calculation are

248 difficult to quantify but are perhaps within 0.3 to 0.5 log units (see discussion in Stagno and Frost
249 2010).

250 **Comparison of the flank method and EELS**

251 We measured a maximum of 25 garnets per experimental sample with the flank method. The
252 uncertainty of ± 0.02 is an empirically proven 1σ error according to the calibration of the method
253 (Höfer and Brey 2007). Calculated 2σ errors were ± 0.04 except for MaLm11 (± 0.06). We
254 performed a maximum of nine EELS measurements per phase per sample. We found that our EELS
255 measurements required a total iron content of at least 5 wt% to gain a sufficient signal-to-noise
256 ratio in the spectra for reliable quantification. We obtained accurate EELS results for three samples:
257 MaLm1, MaLm9 and MaLm11.

258 The results of the two analytical methods overlap within 2σ and show a similar correlation between
259 fO_2 and $Fe^{3+}/\Sigma Fe$ in our experimental charges. However, EELS results of our garnets seem to
260 indicate slightly higher ferric iron contents compared to flank method results, a trend that is also
261 evident in the dataset of Malaspina et al. (2009). One possible explanation for this slight
262 discrepancy could be that the higher number of EPMA measurements per phase more easily
263 compensates for statistical spikes than the comparably lower number of EELS measurements. A
264 possible zonation of our garnets in a μm-range would have been detected during flank method
265 measurements and this would have led to much higher errors than ± 0.04. If any zonation existed
266 at smaller (i.e., nm) scales, it may not have been detected and may have led to average values,
267 whereas EELS analyses would have been able to distinguish these different garnet regions. Another
268 explanation for the higher EELS results might be due to a slight oxidation of our TEM samples
269 during preparation at least on the surface of the lamellae. Nevertheless, ultramicrotomy is
270 considered to prevent a chemical alteration of samples, which was the reason to choose this

preparation technique. Furthermore, the low 1σ error of 0.02 for the flank method is based on a calibration with garnets containing 6 to 21 wt% total iron. Some of the garnets in the present study have even lower iron contents so that the error may be larger in some samples. Moreover, our EELS results agree well with the corresponding values by Rohrbach et al. (2007).

Overall, both measurement techniques lead to comparable results within 2σ and can therefore be used for the successful determination of $Fe^{3+}/\Sigma Fe$. The choice of a technique should therefore rather depend on the available time span, sample amount and desired spatial resolution. One of the main advantages of the EELS method however is, that non-cubic crystals like pyroxenes can be analyzed.

All $Fe^{3+}/\Sigma Fe$ determinations were additionally compared with $Fe^{3+}/\Sigma Fe$ calculated by charge balance calculations. The results fit surprisingly well and agree within 2σ errors both with EELS and flank measurements (Table 3 and Supplementary material, Table S4).

$Fe^{3+}/\sum Fe$ in majoritic garnets and clinopyroxenes

The electron microprobe flank method yields slightly lower $Fe^{3+}/\Sigma Fe$ contents than corresponding EELS measurements (Fig. 2, Table 3) but agree within 2σ uncertainty ($Fe^{3+}/\Sigma Fe$ flank: 0.07(6); $Fe^{3+}/\Sigma Fe$ EELS: 0.11(4), and within 2σ of 0.13(2) determined by Rohrbach et al. (2011). These values represent the minimum $Fe^{3+}/\Sigma Fe$ at metal saturated conditions at 10 GPa. Our results are within the general trend regarding the extent of majorite substitution with increasing pressures as illustrated in Figure 3.

The two effects that are responsible for increasing $Fe^{3+}/\Sigma Fe$ in garnet are increasing pressure and increasing fO_2 (Fig. 4). Experimental metal saturated samples (this study and Rohrbach et al., 2007; IW-0.5 to IW-1.3) define the increase in $Fe^{3+}/\Sigma Fe$ at minimum fO_2 due to disproportionation of FeO, majoritic garnets from slightly more oxidized environments (this study; Woodland and Koch

2003, IW+1.4 to IW+2.9 and Kiseeva et al. 2018, IW-0.3 to IW+3) are systematically shifted to the left of the trend (Fig. 4). Natural non-majoritic garnets span a similar range in $Fe^{3+}/\Sigma Fe$ than the experimental samples.

The clinopyroxenes in our samples tend to have a higher $Fe^{3+}/\Sigma Fe$ content than the majorites, which is in line with results from natural samples by Lazarov et al. (2009) but different to earlier studies where clinopyroxenes had higher $Fe^{3+}/\Sigma Fe$ than the coexisting garnet/majorite (Canil and O'Neill 1996; Rohrbach et al., 2007). One possible explanation might be that the $Fe^{3+}/\Sigma Fe$ in clinopyroxenes is more dependent on bulk composition and Mg# than in garnets. Since the correlation of fO_2 and clinopyroxene has not been systematically studied so far, we cannot draw definite conclusions.

Discussion

Correlation of oxygen fugacity with analyzed $Fe^{3+}/\Sigma Fe$ contents of garnets and clinopyroxenes

All $Fe^{3+}/\Sigma Fe$ measurements using both analytical techniques show a positive correlation with the calculated fO_2 of our samples equilibrated at the same P and T (Fig. 5).

High oxygen fugacities therefore correlate with high ferric iron contents and decrease at more reducing conditions until metal saturation is reached. This is evidence for the fact that our experimental approach as well as ferric iron measurements were successful. Our most reduced and metal saturated sample MaLm11 shows $Fe^{3+}/\Sigma Fe$ between 0.07(6) and 0.11(4) measured by the flank method and EELS (2σ). Our clinopyroxenes measured with EELS show the same positive correlation between $Fe^{3+}/\Sigma Fe$ and fO_2 at slightly higher ferric iron contents. In order to explain the ferric iron content despite metal saturation of MaLm11, disproportionation must be the dominant

process, because no Fe_2O_3 was added and no carbonated fluid or melt was involved, perhaps contrary to the natural samples examined by Kiseeva et al. (2018). We expect to see a correlation between $Fe^{3+}/\Sigma Fe$ and fO_2 natural samples as well, but only if a group of garnet or pyroxene equilibrated at roughly the same P, T and chemical environment. To test this hypothesis, we divided the Ekati garnet dataset of Yaxley et al. (2017) into three subgroups of similar equilibration P and T and found a distinct positive correlation between $Fe^{3+}/\Sigma Fe$ and fO_2 for each subgroup, which is not obvious when plotting the entire dataset (Supplementary Fig. S1). This relationship, however, remains to be tested at other locations.

Application of determined $Fe^{3+}/\sum Fe$ contents to majoritic geobarometers

We performed geobarometric calculations with four different geobarometers from Collerson et al. (2010), Wijbrans et al. (2016), Beyer and Frost (2017) and Tao et al. (2018). Since all four geobarometric calculations take the majorite substitution into account, every single one can be used to calculate pressures in natural high-pressure garnets or run pressures of high P-T-experiments. Two of the geobarometers employ a distinct term for ferric iron (Beyer and Frost 2017; Tao et al. 2018).

The geobarometer by Collerson et al. (2010) describes the extent of majoritic substitution as excess of Si and Ti on the octahedral site of garnet and the respective depletion in Al^{3+} and Cr^{3+}. This geobarometers is also dependent on the Na content but does not include the ferric iron content. The geobarometer by Tao et al. (2018) is based on the geobarometer by Collerson et al. (2010), but only accounts for excess Si on the octahedral site of majorite and for the respective depletion of Al^{3+}, Cr^{3+} and Fe^{3+}. The geobarometer by Beyer and Frost (2017) is the most complex model considering the normal majorite substitution ($Al^{3+} = Si^{4+} + Mg^{2+}$) the Na-majorite substitution ($Mg^{2+} + Al^{3+} = Si^{4+} + Na^{+}$) and accounts for Fe^{3+}, Cr^{3+}, Ti^{4+} and Ca^{2+} contents in majorite. The pressure calculated

by the geobarometer of Wijbrans et al. (2016) for peridotitic compositions solely depends on excess Si^{4+} on the octahedral site and on the Cr^{3+} content of the majorite.

The geobarometer that results in the best fit for our majorites with low ferric iron and low Na contents is the one by Wijbrans et al. (2016) that leads to pressures within a mean ΔP of 0.9 GPa from our experimental pressure of 10 GPa (Fig. 6). We note, however, that the experiments of Wijbrans et al. (2016) were performed using the same experimental equipment as the present study and thus on the same pressure calibration. The dataset used by Wijbrans et al. (2016) to calibrate the barometer is much larger than so we do not expect a large bias of the results.

When we use geobarometry on the experimental majorites of Rohrbach et al. (2011) which have a high total FeO content as well as rather high Na^{+} and ferric iron contents, it seems important to apply a geobarometer which reflect this chemical complexity. The Tao et al. (2018) calibration reproduces experimental run pressures best for this dataset but the Collerson et al. (2010) and Beyer and Frost (2017) geobarometers are also well suited for these rather special majorites. The calibration of Wijbrans et al. (2016) for peridotitic compositions shows rather large pressure discrepancies if applied to this dataset (Supplementary material, Fig. S2).

All four majorite geobarometers agree well with pressures calculated via Al-in-orthopyroxene barometry for garnet peridotites by Woodland and Koch (2003). We have chosen only the highest pressure garnets from the dataset for this comparison. These high pressure garnets have a low concentration of Fe^{3+} and Na^{+} and are only slightly majoritic. (Supplementary material, Fig. S3).

Based on the analysis above we would recommend to apply all geobarometers to the sample of interest. For garnets with low total Fe and presumably low Fe^{3+} (like many natural garnets) it seems acceptable to calculate pressures without knowing the precise ferric iron content.

Implications

Our results confirm that two factors determine the $Fe^{3+}/\Sigma Fe$ in majoritic garnets and high pressure pyroxenes. Metal saturated low fO_2 experimental garnets and pyroxenes set the minimum $Fe^{3+}/\Sigma Fe$ at a given pressure and higher fO_2 raises the $Fe^{3+}/\Sigma Fe$ additionally. We furthermore conclude that both TEM-EELS and the EPMA flank method for the quantitative measurement of ferric iron in silicate minerals yield comparable results within 2σ. Measurements with the "flank method" are much faster and set-up of the method is relatively straight forward when a set of standards with independently measured $Fe^{3+}/\Sigma Fe$ ratios is available. However, EMPA measurements cannot resolve possible nanoscale heterogeneities of measured samples, and the flank method can only be used for garnets, amphiboles and glasses. TEM-EELS on the other hand has a much higher spatial resolution on a nm-scale and can be applied to a variety of non-cubic minerals such as orthopyroxene and clinopyroxene. Nevertheless, TEM measurements and sample preparations are far more time-consuming and allow to measure only a limited numbers of grains. We would like to emphasize that a correct quantitative measurement of ferric iron in garnets is important not only for its accuracy but also for some geobarometric applications and to model the deeper upper mantle and below.

Acknowledgments

We thank Maik Trogisch and Ursula Heitmann for the preparation of samples and Beate Schmitte for helping with the EPMA analysis. Furthermore, we thank Clemens Prescher for providing his MATLAB® script EELSA for the quantification of our EELS spectra. We thank Christian Liebske and an anonymous reviewer for thorough reviews and Sylvie Demouchy for helpful comments and editorial handling. This work was financially supported by the DFG (SFB TRR 170).

References

Akaogi, M., and Akimoto, S. (1979) High-pressure phase equilibria in a garnet lherzolite, with special reference to Mg^{2+}-Fe^{2+} partitioning among constituent minerals. Physics of the Earth and Planetary Interiors, 19, 31–51.

Akaogi, M., and Akimoto, S. (1977) Pyroxene-garnet solid-solution equilibria in the systems $Mg_4Si_4O_{12}$-$Mg_3Al_2Si_3O_{12}$ and $Fe_4Si_4O_{12}$-$Fe_3Al_2Si_3O_{12}$ at high pressures and temperatures. Physics of the Earth and Planetary Interiors, 15, 90–106.

Ballhaus, C., Berry, R.F., and Green, D.H. (1991) High pressure experimental calibration of the olivine-orthopyroxene-spinel oxygen geobarometer: implications for the oxidation state of the upper mantle. Contributions to Mineralogy and Petrology, 107, 27–40.

Ballhaus, C. (1993) Redox states of lithospheric and asthenospheric upper mantle. Contributions to Mineralogy and Petrology, 114, 331–348.

Ballhaus, C., and Frost, R.B. (1994) The generation of oxidized CO_2-bearing basaltic melts from reduced CH_4-bearing upper mantle sources. Geochimica et Cosmochimica Acta, 58, 4931–4940.

Ballhaus, C., (1995) Is the upper mantle metal-saturated? Earth and Planetary Science Letters, 132, 75–86.

Beyer, C., and Frost, D.J. (2017) The depth of sub-lithospheric diamond formation and the redistribution of carbon in the deep mantle. Earth and Planetary Science Letters, 461, 30–39.

Brey, G.P., and Köhler, T. (1990) Geothermobarometry in Four-phase Lherzolites II. New Thermobarometers, and Practical Assessment of Existing Thermobarometers. Journal of Petrology, 31, 1353–1378.

Canil, D., and O'Neill, H.S.C. (1996) Distribution of Ferric Iron in some Upper-Mantle Assemblages. Journal of Petrology, 37, 609–635.

Collerson, K.D., Williams, Q., Kamber, B.S., Omori, S., Arai, H., and Ohtani, E. (2010) Majoritic garnet: A new approach to pressure estimation of shock events in meteorites and the encapsulation of sub-lithospheric inclusions in diamond. Geochimica et Cosmochimica Acta, 74, 5939–5957.

Colliex, C., Manoubi, T., and Ortiz, C. (1991) Electron-energy-loss-spectroscopy near-edge fine structures in the iron-oxygen system. Physical Review B, 44, 11402–11411.

Creighton, S., Stachel, T., Matveev, S., Höfer, H., McCammon, C., and Luth, R.W. (2009) Oxidation of the Kaapvaal lithospheric mantle driven by metasomatism. Contributions to Mineralogy and Petrology, 157, 491.

Creighton, S., Stachel, T., Eichenberg, D., and Luth, R.W. (2010) Oxidation state of the lithospheric mantle beneath Diavik diamond mine, central Slave craton, NWT, Canada. Contributions to Mineralogy and Petrology, 159, 645–657.

Dasgupta, R., and Hirschmann, M.M. (2006) Melting in the Earth's deep upper mantle caused by carbon dioxide. Nature, 440, 659–662.

Dasgupta, R., and Hirschmann, M.M. (2010) The deep carbon cycle and melting in Earth's interior. Earth and Planetary Science Letters, 298, 1–13.

Eggler, D.H., Mysen, B.O., Hoering, T.C., and Holloway, J.R. (1979) The solubility of carbon monoxide in silicate melts at high pressures and its effect on silicate phase relations. Earth and Planetary Science Letters, 43, 321–330.

Enders, M., Speer, D., Maresch, W.V., and McCammon, C. (2000) Ferric/ferrous iron ratios in sodic amphiboles: Mössbauer analysis, stoichiometry-based model calculations and the high-resolution microanalytical flank method. Contributions to Mineralogy and Petrology, 140, 135–147.

Foley, S.F. (2011) A Reappraisal of Redox Melting in the Earth's Mantle as a Function of Tectonic Setting and Time. Journal of Petrology, 52, 1363–1391.

Frost, D.J., Liebske, C., Langenhorst, F., McCammon, C., Trønnes, R.G., and Rubie, D.C. (2004) Experimental evidence for the existence of iron-rich metal in the Earth's lower mantle. Nature, 428, 409–412.

Frost, D.J., and McCammon, C.A. (2008) The Redox State of Earth's Mantle. Annual Review of Earth and Planetary Sciences, 36, 389–420.

Gaetani, G.A., and Grove, T.L. (1998) The influence of water on melting of mantle peridotite. Contributions to Mineralogy and Petrology, 131, 323–346.

Garvie, L.A.J., Craven, A.J., and Brydson, R. (1994) Use of electron-energy loss near-edge fine structure in the study of minerals. American Mineralogist, 79, 411–425.

Haggerty, S.E., and Sautter, V. (1990) Ultradeep (Greater Than 300 Kilometers), Ultramafic Upper Mantle Xenoliths. Science, 248, 993.

443 Höfer, H.E.., Weinbruch, S., McCammon, C.A., and Brey, G.P. (2000) Comparison of two
444 electron probe microanalysis techniques to determine ferric iron in synthetic wüstite
445 samples. European Journal of Mineralogy, 12, 63–71.

446 Höfer, H.E. (2002) Quantification of Fe^{2+}/Fe^{3+} by Electron Microprobe Analysis – New
447 Developments. Hyperfine Interactions, 144, 239–248.

448 Höfer, H.E., and Brey, G.P. (2007) The iron oxidation state of garnet by electron microprobe: Its
449 determination with the flank method combined with major-element analysis. American
450 Mineralogist, 92, 873–885.

451 Irifune, T. (1987) An experimental investigation of the pyroxene-garnet transformation in a
452 pyrolite composition and its bearing on the constitution of the mantle. Physics of the Earth
453 and Planetary Interiors, 45, 324–336.

454 Kiseeva, E.S., Vasiukov, D.M., Wood, B.J., McCammon, C., Stachel, T., Bykov, M., Bykova, E.,
455 Chumakov, A., Cerantola, V., Harris, J.W., and Dubrovinsky, L. (2018) Oxidized iron in
456 garnets from the mantle transition zone. Nature Geoscience, 11, 144–147.

457 Klemme, S., and Fumagalli, P. (2015) Mineralogy of the Earth: Phase Transitions and
458 Mineralogy of the Upper Mantle. In Treatise on Geophysics pp. 7–31.

459 Klemme, S., and O'Neill, H.St.C. (2000) The near-solidus transition from garnet lherzolite to
460 spinel lherzolite. Contributions to Mineralogy and Petrology, 138, 237–248.

461 Kohlstedt, D.L., Keppler, H., and Rubie, D.C. (1996) Solubility of water in the α, β and γ phases
462 of $(Mg,Fe)_2SiO_4$. Contributions to Mineralogy and Petrology, 123, 345–357.

463 Kushiro, I., Syono, Y., and Akimoto, S. (1968) Melting of a peridotite nodule at high pressures
464 and high water pressures. Journal of Geophysical Research (1896-1977), 73, 6023–6029.

465 Lazarov, M., Woodland, A.B., and Brey, G.P. (2009) Thermal state and redox conditions of the
466 Kaapvaal mantle: A study of xenoliths from the Finsch mine, South Africa. Proceedings of
467 the 9th International Kimberlite Conference, 112, 913–923.

468 Li, X., Song, S., Zhang, L., and Höfer, E.H. (2018) Application of microprobe-based flank
469 method analysis of Fe^{3+} in garnet of North Qilian eclogite and its geological implication.
470 Science Bulletin, 63, 300–305.

471 Locock, A.J. (2008) An Excel spreadsheet to recast analyses of garnet into end-member
472 components, and a synopsis of the crystal chemistry of natural silicate garnets. Computers
473 & Geosciences, 34, 1769–1780.

474 Luth, R.W., Virgo, D., Boyd, F.R., and Wood, B.J. (1990) Ferric iron in mantle-derived garnets:
475 Implications for thermobarometry and for the oxidation state of the mantle. Contributions
476 to Mineralogy and Petrology, 104, 56–72.

477 Luth, R.W., and Canil, D. (1993) Ferric iron in mantle-derived pyroxenes and a new
478 oxybarometer for the mantle. Contributions to Mineralogy and Petrology, 113, 236–248.

479 Luth, R.W., and Stachel, T. (2014) The buffering capacity of lithospheric mantle: implications for
480 diamond formation. Contributions to Mineralogy and Petrology, 168, 1083.

481 Mackwell, S.J., Kohlstedt, D.L., and Paterson, M.S. (1985) The role of water in the deformation
482 of olivine single crystals. Journal of Geophysical Research: Solid Earth, 90, 11319–11333.

Malaspina, N., Poli, S., and Fumagalli, P. (2009) The Oxidation State of Metasomatized Mantle Wedge: Insights from C–O–H-bearing Garnet Peridotite. Journal of Petrology, 50, 1533–1552.

Malaspina, N., Scambelluri, M., Poli, S., van Roermund, H.L.M., and Langenhorst, F. (2010) The oxidation state of mantle wedge majoritic garnet websterites metasomatised by C-bearing subduction fluids. Earth and Planetary Science Letters, 298, 417–426.

McCammon, C. (1997) Perovskite as a possible sink for ferric iron in the lower mantle. Nature, 387, 694–696.

McCammon, C.A., and Ross, N.L. (2003) Crystal chemistry of ferric iron in (Mg,Fe)(Si,Al)O_3 majorite with implications for the transition zone. Physics and Chemistry of Minerals, 30, 206–216.

McCammon, C., and Kopylova, M.G. (2004) A redox profile of the Slave mantle and oxygen fugacity control in the cratonic mantle. Contributions to Mineralogy and Petrology, 148, 55–68.

McGuire, A.V., Francis, C.A., and Dyar, M.D. (1992) Mineral standards for electron microprobe analysis of oxygen. American Mineralogist, 77, 1087–1091.

O'Neill, H.St.C., Rubie, D.C., Canil, D., Geiger, C.A., Ross, C.R., Seifert, F., and Woodland, A.B. (1993a) Ferric Iron in the Upper Mantle and in Transition Zone Assemblages: Implications for Relative Oxygen Fugacities in the Mantle. In: E. Takahashi, R. Jeanloz, and D. Rubie, Eds., Geophysical Monograph Series pp. 73–88. American Geophysical Union, Washington D. C..

O'Neill, H.St.C., C.A. McCammon, Canil, D., Rubie, D.C., Ross, C.R., and Seifert, F. (1993b) Mössbauer spectroscopy of mantle transition zone phases and determination of minimum Fe^{3+} content. American Mineralogist, 78, 456–460.

Palme, H., and O'Neill, H.St.C. (2007) Cosmochemical Estimates of Mantle Composition. In: H.D. Holland and K.K. Turekian, Eds., Treatise on Geochemistry pp. 1–38. Pergamon, Oxford.

Pearson, D.G., Brenker, F.E., Nestola, F., McNeill, J., Nasdala, L., Hutchison, M.T., Matveev, S., Mather, K., Silversmit, G., Schmitz, S., and others (2014) Hydrous mantle transition zone indicated by ringwoodite included within diamond. Nature, 507, 221–224.

Prescher, C., Langenhorst, F., Dubrovinsky, L.S., Prakapenka, V.B., and Miyajima, N. (2014) The effect of Fe spin crossovers on its partitioning behavior and oxidation state in a pyrolitic Earth's lower mantle system. Earth and Planetary Science Letters, 399, 86–91.

Rankenburg, K., Lassiter, J.C., and Brey, G. (2004) Origin of megacrysts in volcanic rocks of the Cameroon volcanic chain – constraints on magma genesis and crustal contamination. Contributions to Mineralogy and Petrology, 147, 129–144.

Ringwood, A.E. (1967) The pyroxene-garnet transformation in the earth's mantle. Earth and Planetary Science Letters, 2, 255–263.

Ringwood, A.E., and Major, A. (1971) Synthesis of majorite and other high pressure garnets and perovskites. Earth and Planetary Science Letters, 12, 411–418.

Rohrbach, A., Ballhaus, C., Golla–Schindler, U., Ulmer, P., Kamenetsky, V.S., and Kuzmin, D.V. (2007) Metal saturation in the upper mantle. Nature, 449, 456–458.

525 Rohrbach, A., and Schmidt, M.W. (2011) Redox freezing and melting in the Earth's deep mantle
526 resulting from carbon–iron redox coupling. Nature, 472, 209–212.

527 Rohrbach, A., Ballhaus, C., Ulmer, P., Golla-Schindler, U., and Schönbohm, D. (2011)
528 Experimental Evidence for a Reduced Metal-saturated Upper Mantle. Journal of Petrology,
529 52, 717–731.

530 Sautter, V., Haggerty, S.E., and Field, S. (1991) Ultradeep (>300 Kilometers) Ultramafic
531 Xenoliths: Petrological Evidence from the Transition Zone. Science, 252, 827.

532 Sokol, A.G., Palyanov, Y.N., Kupriyanov, I.N., Litasov, K.D., and Polovinka, M.P. (2010) Effect
533 of oxygen fugacity on the H_2O storage capacity of forsterite in the carbon-saturated
534 systems. Geochimica et Cosmochimica Acta, 74, 4793–4806.

535 Stagno, V., and Frost, D.J. (2010) Carbon speciation in the asthenosphere: Experimental
536 measurements of the redox conditions at which carbonate-bearing melts coexist with
537 graphite or diamond in peridotite assemblages. Earth and Planetary Science Letters, 300,
538 72–84.

539 Stagno, V., Ojwang, D.O., McCammon, C.A., and Frost, D.J. (2013) The oxidation state of the
540 mantle and the extraction of carbon from Earth's interior. Nature, 493, 84–88.

541 Tao, R., Fei, Y., Bullock, E.S., Xu, C., and Zhang, L. (2018) Experimental investigation of Fe^{3+} -
542 rich majoritic garnet and its effect on majorite geobarometer. Geochimica et Cosmochimica
543 Acta, 225, 1–16.

544 Taylor, W.R., and Green, D.H. (1988) Measurement of reduced peridotite-C-O-H solidus and
545 implications for redox melting of the mantle. Nature, 332, 349–352.

546 Taylor, J.R., Wall, V.J., and Pownceby, M.I. (1992) The calibration and application of accurate
547 redox sensors. American Mineralogist, 77, 284–295.

548 Tsuno, K., Frost, D.J., and Rubie, D.C. (2013) Simultaneous partitioning of silicon and oxygen
549 into the Earth's core during early Earth differentiation. Geophysical Research Letters, 40,
550 66–71.

551 Tumiati, S., Fumagalli, P., Tiraboschi, C., and Poli, S. (2012) An Experimental Study on COH-
552 bearing Peridotite up to 3.2 GPa and Implications for Crust–Mantle Recycling. Journal of
553 Petrology, 54, 453–479.

554 van Aken, P.A., and Liebscher, B. (2002) Quantification of ferrous/ferric ratios in minerals: new
555 evaluation schemes of Fe L_{23} electron energy-loss near-edge spectra. Physics and
556 Chemistry of Minerals, 29, 188–200.

557 van Aken, P.A., Liebscher, B., and Styrsa, V.J. (1998) Quantitative determination of iron
558 oxidation states in minerals using Fe $L_{2,3}$ -edge electron energy-loss near-edge structure
559 spectroscopy. Physics and Chemistry of Minerals, 25, 323–327.

560 Vasilyev, P. (2016) The oxidation state of deeply subducted, altered oceanic crust: an
561 experimental study and the evidence from natural samples. PhD Thesis, Research School of
562 Earth Sciences, The Australian National University.

563 Wijbrans, C.H., Rohrbach, A., and Klemme, S. (2016) An experimental investigation of the
564 stability of majoritic garnet in the Earth's mantle and an improved majorite geobarometer.
565 Contributions to Mineralogy and Petrology, 171.

566 Woodland, A., and Koch, M. (2003) Variation in oxygen fugacity with depth in the upper mantle
567 beneath the Kaapvaal craton, Southern Africa. Earth and Planetary Science Letters, 214,
568 295–310.

569 Woodland, A.B., and O'Neill, H.St.C. (1993) Synthesis and stability of $Fe_3^{2+}Fe_2^{3+}Si_3O_{12}$ garnet
570 and phase relations with $Fe_3Al_2Si_3O_{12}$-$Fe_3^{2+}Fe_2^{3+}Si_3O_{12}$ solutions. American Mineralogist,
571 78, 1002–1015.

572 Woodland, A.B., and O'Neill, H.St.C. (1997) Thermodynamic data for Fe-bearing phases
573 obtained using noble metal alloys as redox sensors. Geochimica et Cosmochimica Acta, 61,
574 4359–4366.

575 Yaxley, G.M., Berry, A.J., Kamenetsky, V.S., Woodland, A.B., and Golovin, A.V. (2012) An
576 oxygen fugacity profile through the Siberian Craton — Fe K-edge XANES determinations
577 of $Fe^{3+}/\sum Fe$ in garnets in peridotite xenoliths from the Udachnaya East kimberlite. Lithos,
578 140–141, 142–151.

579 Yaxley, G.M., Berry, A.J., Rosenthal, A., Woodland, A.B., and Paterson, D. (2017) Redox
580 preconditioning deep cratonic lithosphere for kimberlite genesis – evidence from the central
581 Slave Craton. Scientific Reports, 7.

582 Zhang, C., Almeev, R.R., Hughes, E.C., Borisov, A.A., Wolff, E.P., Höfer, H.E., Botcharnikov,
583 R.E., and Koepke, J. (2018) Electron microprobe technique for the determination of iron
584 oxidation state in silicate glasses. American Mineralogist, 103, 1445–1454.

585 **Figure captions**

Figure 1 Backscattered electron (BSE) images of run products. a) Carbonate melt containing sample MaLm2 with garnet-clusters (Grt) and orthopyroxene (Opx). b) Close-up of sample MaLm2 with magnesite (Mgs) and carbonatite melt (C. melt). c) Sample MaLm6 with clinopyroxene-clusters (Cpx). d) Overview of sample MaLm11 with Fe-Ir metal phase with high Fe content. e) Close-up of MaLm11 with garnet and Fe-Ir metal phase. f) Sample MaLm12 with garnet and clinopyroxene-clusters. Small bright particles in all charges are Ir-Fe metal alloys.

Figure 2 Comparison of electron energy loss spectroscopy (EELS) and flank method measurements. Flank measurements are systematically lower in $Fe^{3+}/\Sigma Fe$ than EELS measurements, although results are within 2σ. The black line represents a 1:1 correlation line.

Figure 3 Extent of majorite substitution as function of pressure in natural and synthetic garnets. The number of Si^{4+} cations per formula unit in garnet increases at pressures higher than ~6 GPa. This increase with pressure is more pronounced in iron rich compositions (Rohrbach et al. 2007).

Figure 4 Influence of pressure and fO_2 on the $Fe^{3+}/\Sigma Fe$ content of garnet. The metal saturated sample MaLm11 plots within the range of earlier studies by Woodland and Koch (2003), Rohrbach et al. (2007) and Kiseeva et al. (2018). Black crosses are literature data of natural high-pressure but non-majoritic garnets by Creighton et al. (2008), Lazarov et al. (2009), Creighton et al. (2010), Yaxley et al. (2012; 2017).

Figure 5 Positive correlation between the fO_2 and the $Fe^{3+}/\Sigma Fe$ contents of our garnets and clinopyroxenes analyzed with EELS and flank method. $Fe^{3+}/\Sigma Fe$ contents from both analytical procedures are comparable within 2σ. The maximum uncertainty on the fO_2 is ± 0.5 log units.

606 Figure 6 Four different geobarometers by Collerson et al. (2010), Wijbrans et al. (2016), Beyer and
607 Frost (2017) and Tao et al. (2018) applied to our experimental dataset. All calculated pressures are
608 comparable within errors when using the EELS results instead of the flank results.

609

610

611

612

613

614

615

620

623 **Tables**

624 Table 1 Primitive mantle composition and experimental starting composition analogues.

Oxide (wt%)	Palme and O'Neill, 2003	Rohrbach et al., 2011	Irifune, 1987	This study
SiO_2	45.40	47.50	50.36	46.54
MgO	36.77	14.70	22.80	35.24
FeO	8.10	26.20	3.46	8.20
Al_2O_3	4.49	6.45	11.38	5.10
CaO	3.65	3.80	9.24	4.14
Na_2O	0.50	0.50	1.03	0.57
NiO	0.19	-	-	0.21
TiO_2	-	0.29	0.58	-

Cr_2O_3	-	0.56	1.16	-
Mg#	0.89	0.36	0.88	0.81

The composition by Palme and O'Neill (2003) correlates with the major element composition of the PM (Mg# of 0.89). Rohrbach et al. (2011) depleted the composition by Palme and O'Neill (1993) by 30% in its normative olivine content and raised the molar Mg# to around 0.5. Irifune (1987) used a rather basaltic starting composition, that was created by subtraction of an olivine from a pyrolitic composition. The Mg# used was similar to the one proposed for the PM (Palme and O'Neill, 2003). The starting composition from this study was based on the PM composition by Palme and O'Neill (1993), however, 10% of normative olivine were subtracted. All three starting compositions are calculated starting compositions which is why no errors are stated here.

This is the peer-reviewed, final accepted version for American Mineralogist, published by the Mineralogical Society of America.
The published version is subject to change. Cite as Authors (Year) Title. American Mineralogist, in press.
DOI: https://doi.org/10.2138/am-2020-7265. http://www.minsocam.org/

Table 2 Experimental conditions

Experiment	Composition	Capsule material	Temperature (°C)/run duration
MaLm1	SC, 1wt% C	$Au_{80}Pd_{20}$	1500/24 h
MaLm2	SC, 1wt% C	$Au_{80}Pd_{20}$	1550/24 h
MaLm6	SC, 1wt% Si-metal	$Au_{80}Pd_{20}$	1450/24 h
MaLm9	SC	$Au_{80}Pd_{20}$	1550/24 h
MaLm11	SC	$Au_{80}Pd_{20}$ (inner capsule) Fe (outer capsule)	1450/24 h
MaLm12	SC	$Au_{80}Pd_{20}$	1450/24 h

SC corresponds to the starting composition of this study and includes the starting composition (Table 1) plus 5 wt% $C_{18}H_{36}O_2$ and 3 wt% Ir. All experiments were performed at 10 GPa.

This is the peer-reviewed, final accepted version for American Mineralogist, published by the Mineralogical Society of America.
The published version is subject to change. Cite as Authors (Year) Title. American Mineralogist, in press.
DOI: https://doi.org/10.2138/am-2020-7265. http://www.minsocam.org/

Table 3 Average phase compositions, $Fe^{3+}/\Sigma Fe$ and oxygen fugacities

Exp	**MaLm1**				**MaLm2**				**MaLm6**			
Phase	Ol	Cpx	Opx	Grt	Ol	Cpx	Opx	Grt	Ol	Cpx	Opx	Grt
n	17	22	2	14			23	22	9	25	16	25
SiO_2	40.50(47)	56.34(37)	57.75(24)	42.91(46)	-	-	58.64(38)	45.01(30)	41.87(17)	56.77(36)	59.36(27)	44.76(24)
Al_2O_3	0.14(17)	1.73(36)	0.34(11)	21.01(82)	-	-	0.75(14)	20.36(38)	0.03(1)	1.63(28)	0.30(2)	20.31(19)
Fe_2O_3	n.d.	n.d.	n.d.	1.41	-	-	n.d.	0.71	n.d.	n.d.	n.d.	0.77
FeO	n.d.	n.d.	n.d.	6.88	-	-	n.d.	3.70	n.d.	n.d.	n.d.	4.36
FeO*	9.14(33)	5.69(35)	7.08(21)	8.29(36)	-	-	3.08(24)	4.41(35)	4.66(52)	2.51(41)	2.90(55)	5.13(55)
MgO	48.65(68)	23.89(64)	33.96(71)	22.56(53)	-	-	36.84(41)	25.71(35)	53.82(56)	21.06(41)	37.68(44)	24.23(37)
CaO	0.13(7)	10.98(96)	0.43(4)	3.82(19)	-	-	1.42(15)	2.98(18)	0.07(2)	17.53(62)	0.55(8)	4.16(15)
Na_2O	0.06(2)	1.30(11)	0.08(2)	0.14(2)	-	-	0.21(5)	0.11(1)	0.02(2)	1.12(7)	0.09(2)	0.13(1)
NiO	1.82(36)	0.44(10)	0.83(17)	0.17(5)	-	-	0.13(3)	0.03(1)	0.07(2)	0.02(2)	0.03(3)	0.01(1)
Total	100.44	100.37	100.47	98.83	-	-	101.07	98.61	100.54	100.64	100.91	98.73
$Fe^{3+}/\Sigma Fe$ (flank)	-	-	-	0.17(4)	-	-	-	0.16(4)	-	-	-	0.15(4)
n	-	-	-	14	-	-	-	22	-	-	-	25
$Fe^{3+}/\Sigma Fe$ (EELS)	-	0.29(12)	-	0.27(6)	-	-	-	n.d.	-	-	-	n.d.
n	-	9	-	7	-	-	-	-	-	-	-	-
$Fe^{3+}/\Sigma Fe$ (c.b.)	-	-	-	0.28	-	-	-	0.18	-	-	-	0.14
#Mg	0.90	0.88	0.90	0.83	-	-	0.96	0.91	0.95	0.94	0.96	0.89
$\Delta \log fO_2$ [FMQ]	-1.7				-				-1.8			
$\Delta \log fO_2$ [EMOD]	+0.2				-				+0.1			
$\Delta \log fO_2$ [IW]	+3.4				-				+3.3			

This is the peer-reviewed, final accepted version for American Mineralogist, published by the Mineralogical Society of America.
The published version is subject to change. Cite as Authors (Year) Title. American Mineralogist, in press.
DOI: https://doi.org/10.2138/am-2020-7265. http://www.minsocam.org/

Exp	**MaLm9**				**MaLm11**				**MaLm12**			
Phase	Ol	Cpx	Opx	Grt	Ol	Cpx	Opx	Grt	Ol	Cpx	Opx	Grt
n	24	23	3	19	12	2	5	7	20	22	1	21
SiO_2	41.06(22)	57.02(32)	58.65(36)	44.38(66)	41.25(49)	57.34(1)	58.74(42)	43.58(55)	42.19(18)	56.91(23)	59.68	44.41(43)
Al_2O_3	0.05(2)	1.37(7)	0.42(12)	18.73 (1.28)	0.08(5)	1.65(11)	0.34(5)	22.52(94)	0.05(2)	1.70(57)	0.26	20.82(88)
Fe_2O_3	n.d.	n.d.	n.d.	2.25	n.d.	n.d.	n.d.	0.51	n.d.	n.d.	n.d.	0.80
FeO	n.d.	n.d.	n.d.	6.08	n.d.	n.d.	n.d.	6.72	n.d.	n.d.	n.d.	2.84
FeO*	8.82(19)	6.26(47)	5.24(12)	8.33(86)	9.14(1.38)	4.32(10)	5.19(48)	7.23(34)	3.69(27)	1.31(16)	2.51	3.64(32)
MgO	49.72(23)	25.62(78)	34.62(88)	23.87(36)	49.45(1.35)	22.35(44)	34.91(53)	22.31(31)	55.00(33)	20.50(63)	38.47	24.61(78)
CaO	0.11(3)	8.92(66)	1.57(81)	3.22(12)	0.16(20)	14.23(18)	0.97(27)	3.54(14)	0.05(2)	19.21(70)	0.34	4.63(33)
Na_2O	0.07(3)	1.16(6)	0.19(6)	0.13(1)	0.05(3)	1.09(7)	0.16(5)	0.21(4)	0.07(3)	1.29(41)	0.08	0.16(3)
NiO	0.45(4)	0.15(3)	0.15(8)	0.04(1)	0.09(2)	0.04(1)	0.13(5)	0.01(1)	0.06(3)	0.02(2)	0.04	0.01(1)
Total	100.28	100.50	100.84	98.70	100.2	101.02	100.44	99.40	101.11	100.94	101.38	98.28
$Fe^{3+}/\Sigma Fe$ (flank)	-	-	-	0.27(4)	-	-	-	0.07(6)	-	-	-	0.22(4)
n	-	-	-	17	-	-	-	13	-	-	-	19
$Fe^{3+}/\Sigma Fe$ (EELS)	-	0.54(14)	-	0.31(14)	-	0.17(10)	-	0.11(4)	-	-	-	-
n	-	5	-	8	-	9	-	6	-	-	-	-
$Fe^{3+}/\Sigma Fe$ (c.b.)	-	-	-	0.31	-	-	-	0.06	-	-	-	0.26
#Mg	0.91	0.88	0.92	0.84	0.91	0.90	0.92	0.84	0.96	0.97	0.96	0.92
Δlog fO_2 [FMQ]	-0.4				-4.3				-0.5			
Δlog fO_2 [EMOD]	+1.5				-2.4				+1.4			
Δlog fO_2 [IW]	+4.7				+0.9				+4.6			

Average major element analyses in wt%, Mg# and fO_2 of all experiments including olivine (Ol), clinopyroxene (Cpx), orthopyroxene (Opx) and majoritic garnets (Grt). Cation $Fe^{3+}/\Sigma Fe$ (c.b.) values refer to ferric iron contents derived from charge balance calculations (see also Supplementary material, Table S4). Uncertainties of the EPMA measurements are 1σ, errors of the $Fe^{3+}/\Sigma Fe$ values are 2σ. Total FeO of garnet was divided into FeO and Fe_2O_3 according to $Fe^{3+}/\Sigma Fe$ measured by the flank method, other values are reported in Supplementary material, Table 4. n.d. = not determined.*

Figure 1

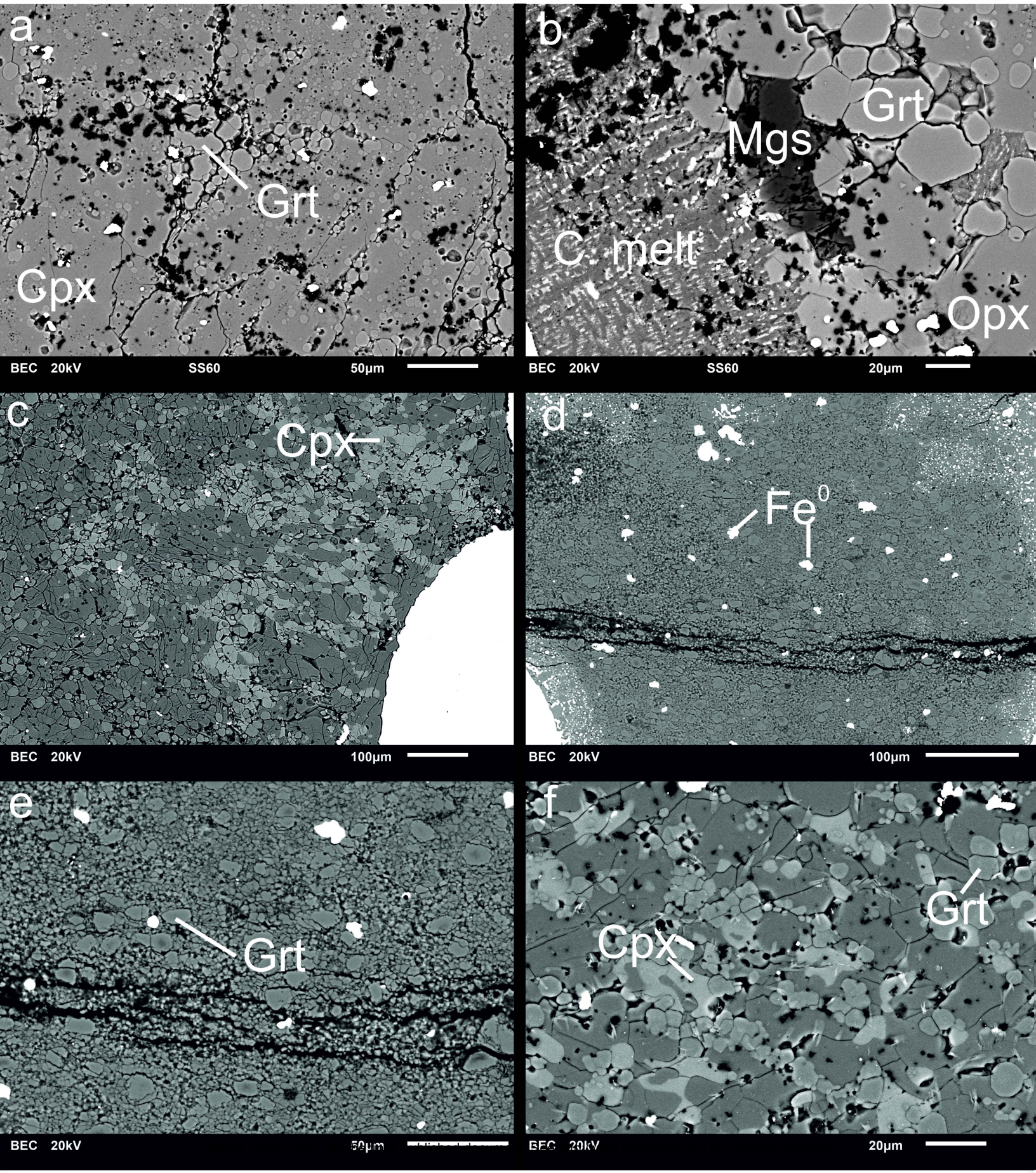

Figure 2

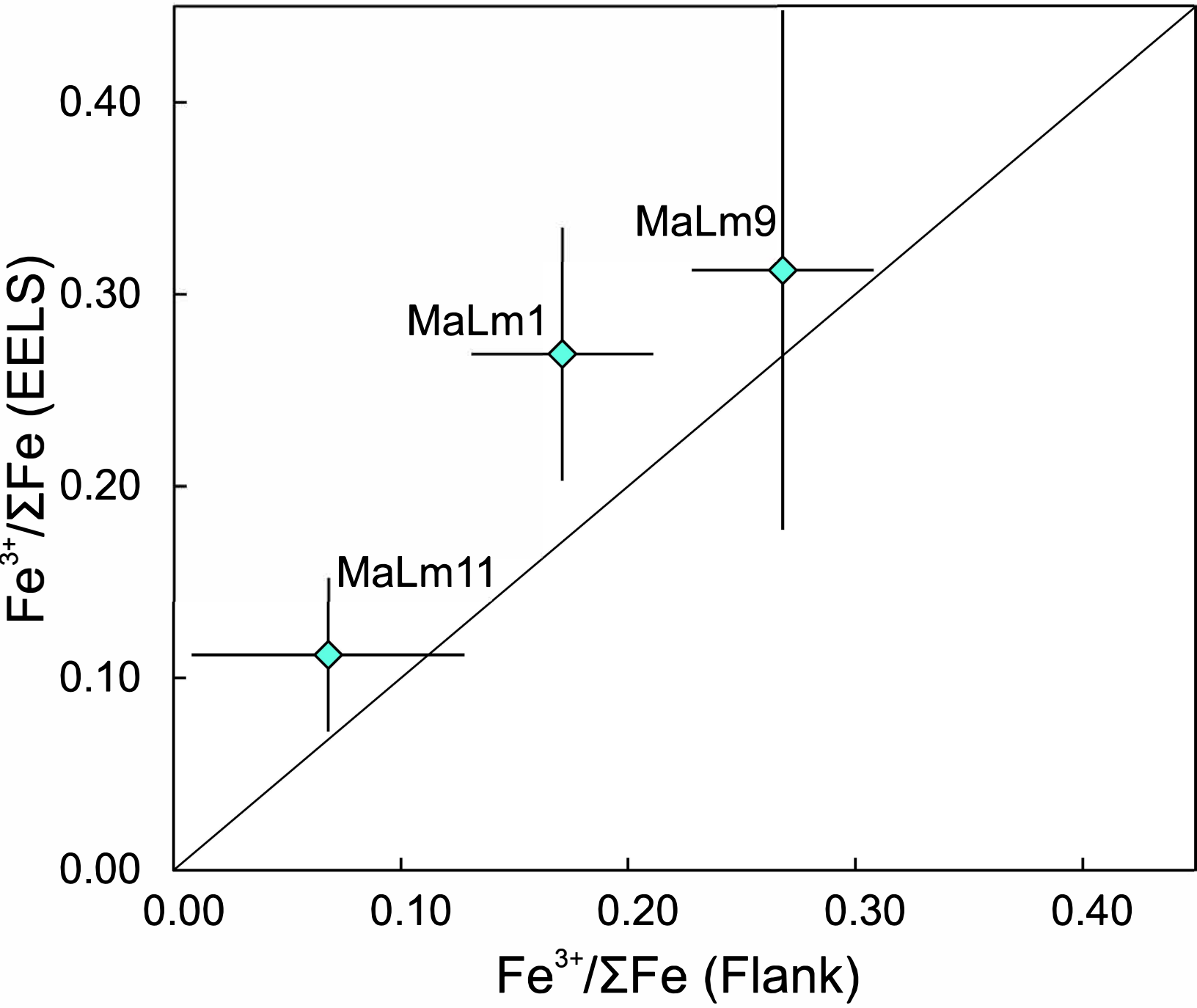

Figure 3

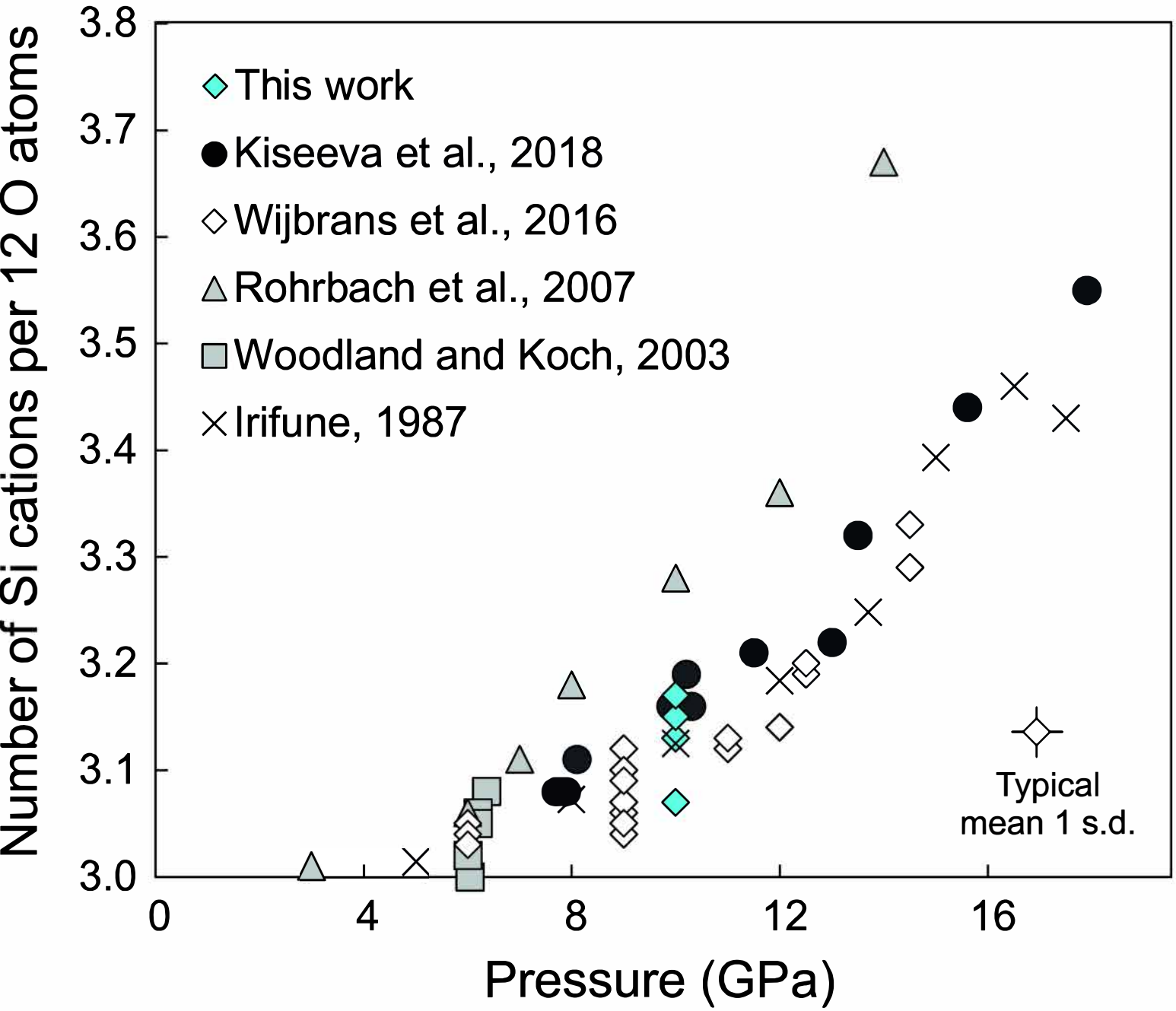

This is the peer-reviewed, final accepted version for American Mineralogist, published by the Mineralogical Society of America.
The published version is subject to change. Cite as Authors (Year) Title. American Mineralogist, in press.
DOI: https://doi.org/10.2138/am-2020-7265. http://www.minsocam.org/

Figure 4

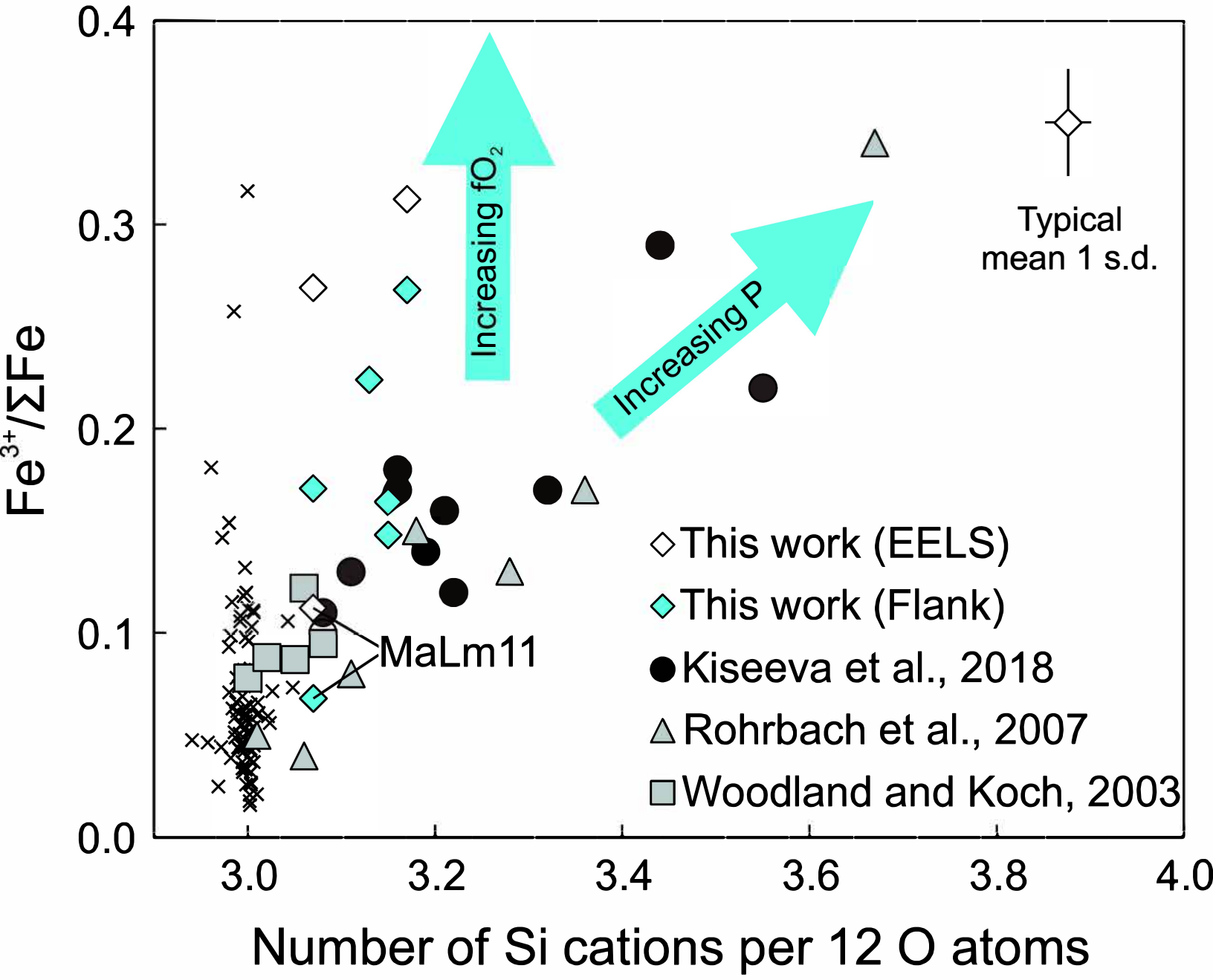

This is the peer-reviewed, final accepted version for American Mineralogist, published by the Mineralogical Society of America.
The published version is subject to change. Cite as Authors (Year) Title. American Mineralogist, in press.
DOI: https://doi.org/10.2138/am-2020-7265. http://www.minsocam.org/

Figure 5

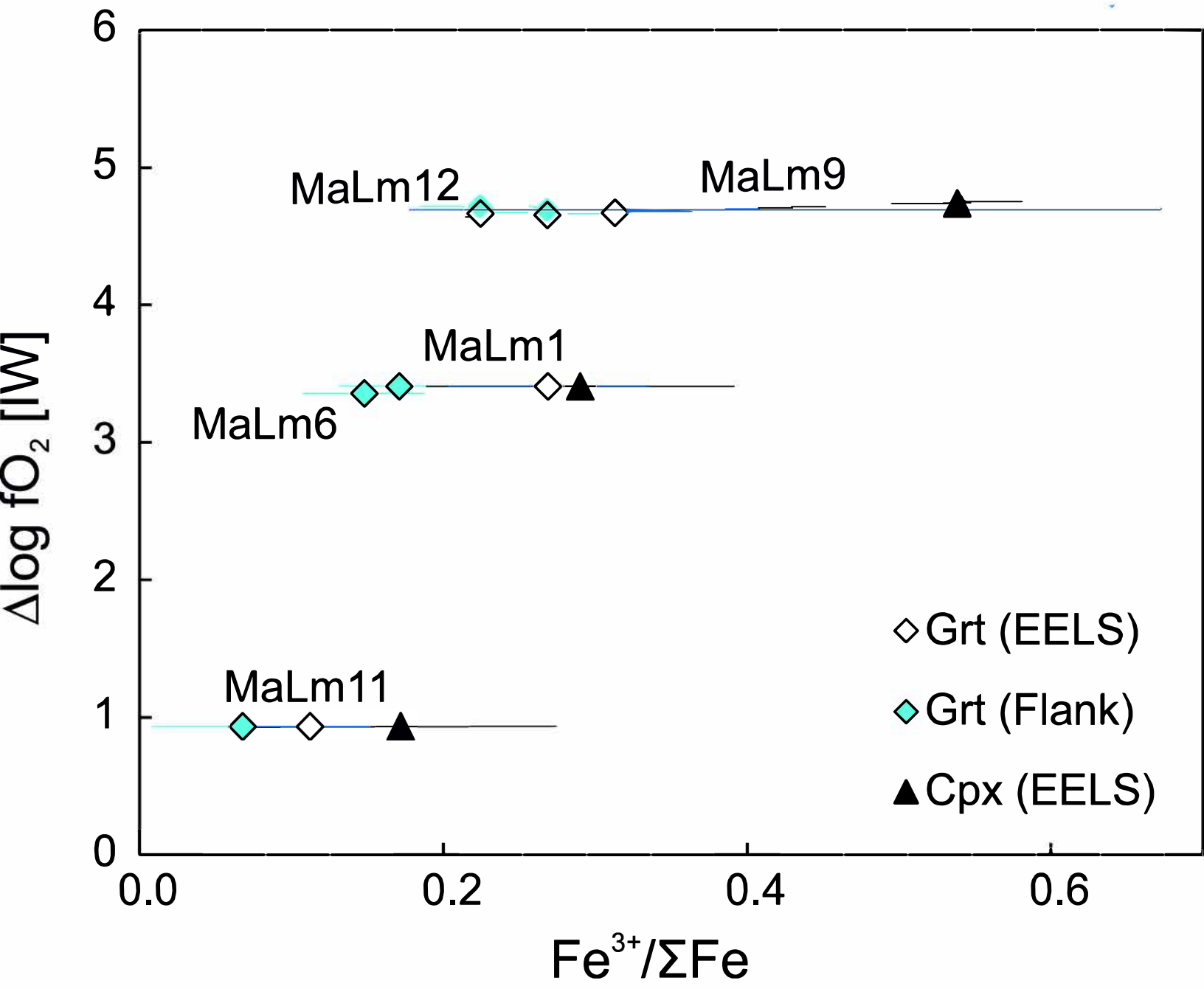

Figure 6